Chemistry – A European Journal

ChemEurJ Chemistry Europe European Chemical Societies Publishing

RESEARCH ARTICLE

High-Pressure Synthesis of a Novel Body-Centered Tetragonal Vanadium Carbide

Elizabeth E. Cote[1] | Tracey L. Nelson[1] | Scott D. Ambos[1] | John Arigbede[1] | Chris Walsh[1] | Rachel E. Bernard[2] | Hanna L. Brooks[2] | Matthew L. Whitaker[3] | James P. S. Walsh[1]

[1]Department of Chemistry, University of Massachusetts Amherst, Amherst, United States | [2]Department of Geology, Amherst College, Amherst, United States | [3]Mineral Physics Institute, Department of Geosciences, Stony Brook University, Stony Brook, United States

Correspondence: James P. S. Walsh (jpswalsh@umass.edu)

Received: 16 October 2025 | **Revised:** 26 March 2026 | **Accepted:** 27 March 2026

Keywords: carbides | high pressure | large volume press | metastable phases | solid-state chemistry

ABSTRACT

High-pressure synthesis is a powerful tool for the discovery of new phases, and can be used to uncover new metastable phases even within well-explored systems. The vanadium–carbon system is one of the most well-studied binary systems due to its importance in steels as well as for its many high-resilience compounds used across industry. We present in situ x-ray diffraction data collected during synthesis experiments carried out between 1.0 and 5.1 GPa in the V–C system at 25 at.% carbon, and we report the synthesis and recovery of a novel metastable body-centered tetragonal carbide, $\epsilon - VC_{y''}$.

1 | Introduction

Transition metal carbides are known for their thermomechanical stability, which can include ultra-high melting points, elevated hardness, and robust chemical inertness. These properties make them useful in extreme environment applications such as high-temperature structural components, high-speed cutting tools, and wear-resistant coatings [1–3]. Group IV–V elements (i.e., Ti, Zr, Hf, V, Nb, Ta) tend to form what are known as interstitial carbides, where carbon atoms occupy the space within the interstitial sites of the metal lattice. These interstitial phases retain metallic properties, but tend to exhibit higher hardness due to the strong and directional M–C covalent bonding (e.g., niobium carbide, NbC), or refractory properties due to very high stability (e.g., hafnium carbide, HfC) [2, 4].

Vanadium carbides are used across a wide range of industrial applications, including as turbine coatings, as grain growth inhibitors in tungsten carbide cermets, and more recently have been explored as catalysts in the hydrogen evolution reaction [5–7]. Historically, vanadium has been well studied as an additive in steels, where the small grains of vanadium carbides or nitrides that form cause a reduction in dislocations, leading to precipitation strengthening [8]. In recent years, the vanadium carbides have also been studied as hydrogen traps to mitigate embrittlement in iron-based steels [9, 10].

The vanadium–carbon binary system was extensively studied from the 1960s to the 1980s, and is characterized by its structural complexity, containing seven experimentally observed phases and many more that have been predicted [11–17]. Figure 1 shows how the seven known vanadium carbides can be classified by the lattice formed by the metal. As with other Group IV–V transition metals, the NaCl-type VC_y structure (Strukturbericht designation: $B1$) is highly stable. This phase is referred to as VC_y and can be described as an interstitial carbide wherein a face-centered cubic (fcc) metal lattice hosts carbon in its octahedral interstitial sites. The $B1$ carbide phases can often accommodate a broad range of substoichiometry at the carbon site, since carbon vacancies can enhance stability by increasing configurational entropy, or by allowing for stoichiometric ordered structures

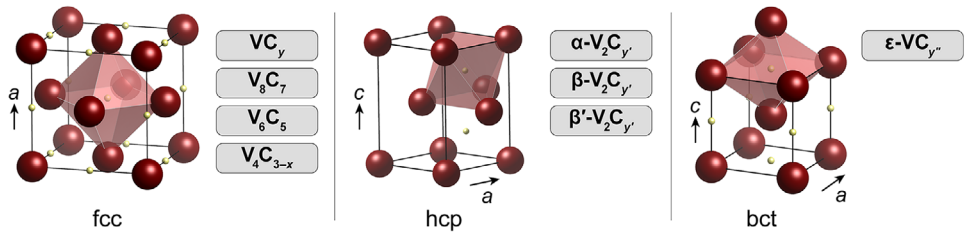

FIGURE 1 | Classification of the known vanadium carbides by metal lattice arrangement. Interstitial carbon sites are depicted as small yellow spheres within the parent lattice of vanadium, which is depicted using red spheres. The carbon environment is illustrated using semitransparent polyhedra. The $B1$ phase (VC_y) and its derivatives can all be described as structures where the vanadium atoms adopt a face-centered cubic (fcc) lattice with the carbon atoms occupying octahedral interstitial sites. The structures differ only in the concentration and ordering of carbon atoms among the octahedral sites. The V_2C phases are instead derived from a hexagonal close-packed lattice of vanadium atoms, with carbon again occupying octahedral interstitial sites. The body-centered tetragonal (bct) phase reported herein is the first example of a vanadium carbide where the vanadium atoms adopt a bct lattice, with carbon atoms occupying tetragonally compressed pseudo-octahedral interstitial sites.

that maximize favorable nearest-neighbor interactions while minimizing unfavorable ones [18]. In other cases, and particularly for the more electron-rich transition metals, substoichiometry can stabilize a phase by reducing the unfavorable population of antibonding orbitals [11]. This is the case for vanadium, where the fully stoichiometric VC_y (i.e., $y = 1$) is unstable under standard conditions, decomposing immediately into $VC_{0.88}$ and graphite. This singles out vanadium as the only Group IV–V transition metal not to exhibit the fully occupied rock salt structure phase [11, 12, 16, 19–21].

Many of the phases reported in the V–C system can be described as ordered derivatives of the $B1$ structure. However, it also contains a number of phases derived from a hexagonal close-packed (hcp) lattice, as seen in Figure 1. These phases, α-V_2C ($Pbcn$), β-$V_2C_{y'}$ ($P6_3/mmc$), and β'-V_2C ($P\bar{3}m1$), appear over a narrow range of composition with 27 < at.% carbon < 34. The most commonly reported phase of the three is β-$V_2C_{y'}$, which can be described as an hcp vanadium lattice with the octahedral interstitial sites randomly occupied (i.e., disordered) [11, 12]. These phases are sometimes represented as $V_2C_{y'}$ to illustrate the variable stoichiometry of carbon, and we will adopt this nomenclature here. With the exception of the small solubility of carbon into vanadium metal (upper limit of 4.3 at.% C at 1923 K), the $V_2C_{y'}$ phases are the most metal-rich compounds in the V–C phase diagram to date [11, 12].

The growth of crystals larger than a few microns is rare for vanadium carbides, with most studies reporting on nanocrystalline or thin film phases [11, 12, 22]. The only reports that detail large single crystals involve the use of the floating zone technique to grow crystals of the $B1$ phase [14, 22, 23]. All other structures have been determined using powder methods on polycrystalline samples [11, 12, 23]. Despite the extensive work carried out on the V–C system, its behavior under high pressure remains unexplored. The only high-pressure study to date uses pressure to sinter a polycrystalline sample of the $B1$ phase at 5.0 GPa [24].

Here we present an experimental investigation of the high-pressure reactivity in the V–C system between 1.0 and 5.1 GPa in the metal-rich region of 25 at.% C. Across all pressures, we recovered large single crystals of the known β-$V_2C_{y'}$ phase, as well as large single crystals of a novel bct vanadium carbide, $\epsilon - VC_{y''}$. We present in situ X-ray diffraction data collected during the high-pressure synthesis, which provides insight into the mechanism of formation of these phases.

2 | Methods

2.1 | High-Pressure Synthesis

All chemicals, unless noted, were used without further purification after receiving them from the supplier. Vanadium metal (2.0885 g, 325 mesh, 99.99%) and graphite (0.1639 g, 99.9995%) were hand-mixed in a 3:1 molar ratio and then transferred to an agate-lined stainless steel jar along with six agate balls (approximately 0.4 g each). The jar was then placed in a Retsch planetary ball mill and the powders were mixed at 250 rpm for 5-min intervals with 10 min rest periods in between. The rotation direction was reversed between each cycle, and the total milling time was 48 h. The ball-milled powder was then pressed into pellets of the appropriate size using stainless steel dyes inside an argon-filled glove box to prevent oxidation. We used COMPRES 10/5 equatorial assemblies in all experiments [25, 26]. The equatorial cells contained an MgO ring window and a TiB_2-doped boronitride (BN) furnace to allow a wider window for in situ x-ray diffraction than can be achieved with the standard assemblies.

High-pressure high-temperature synthesis experiments were performed at beamline 28-ID-D (MAXPD) at the National Synchrotron Light Source II, Brookhaven National Laboratory. A Kawai-type multi-anvil press was used to compress the sample, which was then heated via resistive heating. In a typical synthesis run, the pellet was first compressed to the target pressure, then heated to 1200 K and held at that temperature for 15 min. After each run, the sample was rapidly cooled to room temperature in 8 min or less and then finally decompressed to ambient pressure over 6 h to 8 h. Single crystals were isolated from the product matrix via mechanical separation. X-ray diffraction images were collected in situ ($\lambda = 0.1814$ Å) by a Perkin Elmer area detector with diffraction patterns collected every 10 s. The detector position was calibrated using diffraction from a LaB_6 standard.

2.2 | Crystal Structure Solution

For phase identification and crystal structure solution of the samples recovered to ambient conditions, x-ray diffraction experiments were performed using a Rigaku XtaLAB Synergy-S diffractometer equipped with a HyPix-6000HE detector and using Ag Kα radiation ($\lambda = 0.5594$ Å). All diffraction experiments were performed at room temperature. Reflections were processed with CrysAlis^{Pro} (Rigaku, ver. 1.171.42.63a), and structures were solved in Olex2 (ver. 1.5) using the SHELXT package [27, 28]. Structure models were refined using the least-squares method of SHELXL [28].

2.3 | Electron Backscatter Diffraction

Electron backscatter diffraction (EBSD) mapping was performed on isolated pieces of the recovered sample pellets using a Zeiss SEM 500 VP field emission scanning electron microscope (FE-SEM) at Amherst College. The FE-SEM is equipped with a Zeiss SE2 detector for secondary electron detection and an Oxford Instruments Symmetry S2 detector for EBSD. FE-SEM details and methodology for both SE imaging and EBSD chemistry are detailed in Table S5. The samples were already conductive and therefore were not additionally coated for FE-SEM analysis. Samples were prepared for EBSD by mounting them in epoxy, followed by mechanical polishing with diamond lapping paste down to 1 μm grit size. Following mechanical polishing, samples were then polished in colloidal silica in a Vibromet for 8 h to reduce residual strain from mechanical polishing, then finally washed with dish soap to remove residual colloidal silica. Maps were analyzed within Oxford Instruments post-acquisition processing software Aztec Crystal (Version 3.1).

2.4 | Calculations

Density functional theory calculations to determine the relationship between carbon occupancy and tetragonal distortion in NaCl-type VC_y were carried out with CASTEP v25.1.2 [29]. We sampled 300 carbon vacancy configurations of a 32-V atom $2 \times 2 \times 2$ conventional supercell of VC_y. From each of these configurations, one to three unique distorted structures were generated by shortening one of the lattice vectors by 79% (the approximate distortion seen in experiments). The original cubic structures and their distorted counterparts (1744 structures in total) were then geometry optimized at 0 GPa. For these optimizations lattice angles were constrained to 90 °, while lattice lengths and ionic positions were allowed to relax.

The calculations employed the Perdew–Burke–Ernzerhof (PBE) approach to the generalized gradient approximation of the exchange-correlation functional [30]. The calculations used CASTEP's high-throughput psuedopotential library (QC5), a cutoff energy of 400.0 eV, a maximum Monkhorst–Pack [31] grid spacing of 0.05 Å^{-1}, and finite basis set corrections. The inputs and results of these calculations were managed using the Atomic Simulation Environment (ASE) [32] and the pymatgen [33] library of python packages.

3 | Results and Discussion

We examined the reactivity of vanadium and carbon at the metal-rich composition of 25 at.% carbon in four separate high-pressure synthesis runs carried out at peak pressures ranging from 1.0 to 5.1 GPa, and with heating in all cases to peak temperatures of around 1200 K. Under ambient pressure, this composition is expected to lead to a mixture of stoichiometric V_2C and bcc-V alloyed with a small amount of carbon (see Supporting Information). In all four runs, we recovered single crystals belonging to two distinct phases. The first phase is the hexagonal β-$V_2C_{y'}$ phase ($P6_3/mmc$), which at ambient pressure is known to form in the range of 27.0 < at.% carbon < 34.0 ($0.36 < y' < 0.58$) at temperatures above around 1923 K [11]. The second phase recovered from our high-pressure syntheses was solved to a bct martensite-type structure ($I4/mmm$), which has not been previously reported in this system. Both phases are discussed below, along with a discussion of the in situ X-ray diffraction data collected during the synthesis runs.

3.1 | β-$V_2C_{y'}$

The β-$V_2C_{y'}$ phase adopts the anti-NiAs prototype structure (space group: $P6_3/mmc$, Strukturbericht designation: $L'3_0$), which is the same structure adopted by β-W_2C, β-Ta_2C, and β-Mn_2C [4, 34–36]. This structure can be described as an hcp lattice of vanadium with half of the octahedral interstices randomly occupied by carbon (i.e., a disordered phase) [11, 12]. In the V–C system, this is considered to be a high-temperature phase, with the ordered α-V_2C ($Pbcn$) and β'-V_2C ($P\bar{3}m1$) phases being more stable at temperatures somewhere below 1100 K to 1600 K (the exact temperatures are not known) [11]. It should be noted that the hexagonal carbides are sometimes labeled as NiAs-type ($B8_1$), but the anti-NiAs-type designation is more accurate due to the reversal of the cation and anion coordination (i.e., it is the As atoms that form the hcp lattice in NiAs-type). In our high-pressure experiments, we observe only the disordered β-$V_2C_{y'}$ phase, and do not see evidence of either of the two ordered phases. This could imply that rapid cooling—on the order of seconds or minutes in this case due to the small sample volume—allowed for the recovery of the metastable high-temperature phase, or that this phase is accessible at lower temperatures under compression.

In all of the single crystal samples that we studied, the diffraction datasets exhibited additional weak Bragg reflections from separate domains with practically identical lattice parameters, but with orientation matrices that had no obvious relation to that of the main peaks. This suggests that these reflections came from smaller crystallites attached to the main crystals. Within the primary crystal domains, we saw no evidence of twinning. We also performed scanning electron microscopy, which confirms the presence of smaller crystallites (see Supporting Information). The lattice parameters of the eight samples of β-$V_2C_{y'}$ reported here fall within the relatively narrow ranges of $2.88 < a < 2.91$ Å and $4.56 < c < 4.59$ Å, while the refined carbon occupancy falls in the range$1.02 < y < 1.20$ (33.8–37.4 at.% carbon). These values are consistent with what has been observed in β-$V_2C_{y'}$ samples recovered under ambient pressures, suggesting that the pressures studied herein have a minimal effect on the carbon content in this phase [11, 12].

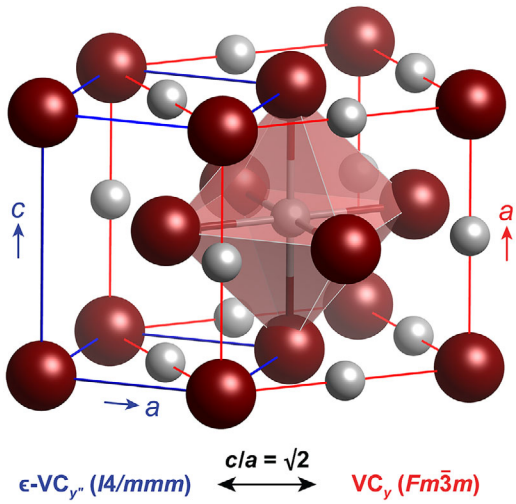

FIGURE 2 | Illustration of the relationship between the tetragonal $\epsilon - VC_{y''}$ structure and the cubic $B1$ phase VC_y. Vanadium atoms are depicted in red and carbon atoms are depicted in gray. The unit cell of the $B1$ phase is shown in red, while that of the martensite structure is shown in blue. The octahedral coordination of the carbon atom at the center of the $B1$ unit cell is highlighted with a red polyhedron. The tetragonal cell is depicted with $c/a = \sqrt{2}$, where the two structures are indistinguishable. In the bct phase, this ratio is below $\sqrt{2}$, leading to a tetragonal compression of the octahedral interstitial site occupied by carbon.

3.2 | $\epsilon - VC_{y''}$

Alongside the hexagonal β-$V_2C_{y'}$ crystals, we also recovered crystals of a novel tetragonal phase that we refer to as $\epsilon - VC_{y''}$. This phase contains vanadium atoms in a bct structure with carbon occupying its pseudo-octahedral interstitial sites. This structure is analogous to the bct martensite structure seen in iron steels (FeC_x, $x < 0.06$) [37], solving to the $I4/mmm$ space group with vanadium and carbon atoms in the (2a) and (2b) Wyckoff positions, respectively. We invoke the term "martensite" here solely to describe the structural prototype of this novel phase, rather than as a descriptor of its mechanism of formation. However, we do find similarities with martensitic growth mechanisms observed in iron steels, as we describe below.

Figure 2 shows how the bct structure is related to the $B1$ structure of VC_y. According to the Bain model, when the c/a ratio of the tetragonal martensite structure is equal to $\sqrt{2}$ (≈ 1.414), then the two structures are identical [38, 39]. At lower/higher ratios, the interstitial sites become tetragonally compressed/elongated, leading to the "pseudo-octahedral" coordination around the carbon atoms. In $\epsilon - VC_{y''}$, the carbon site is tetragonally compressed ($c/a < \sqrt{2}$). The $\epsilon - VC_{y''}$ structure hosts a significant range of substoichiometry at the carbon site, with refinements of the carbon occupancy from x-ray diffraction modeling yielding $0.12 < y'' < 0.36$ (11 − 27 at. % carbon) across our recovered samples.

The crystallization of the hexagonal phase β-$V_2C_{y'}$ from a 25 at.% carbon mixture is consistent with the phase diagram determined for ambient pressures, albeit with the unexpected quenching of the disordered "high-temperature" β-$V_2C_{y'}$ phase.

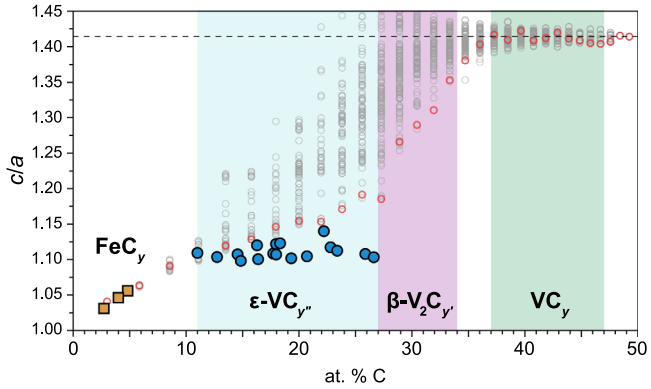

FIGURE 3 | Plot of the c/a ratio as a function of the carbon occupancy for experimental $\epsilon - VC_{y''}$ (blue circles) and iron martensite $FeC_{(x<0.06)}$ (orange squares, taken from Ref. [39]). The dashed line indicates the c/a ratio of $\sqrt{2}$, which corresponds to a face-centered cubic (fcc) lattice (i.e., the $B1$ structure). Shaded regions represent the experimentally known limits of the stability field of the $\epsilon - VC_{y''}$, β-$V_2C_{y'}$, and $B1$ VC_y phases. Open circles represent computationally relaxed structures of the bct phase across the full composition range, with the lowest energy structures plotted in red.

The crystallization of a body-centered tetragonal phase, on the other hand, is a significant departure from the ambient pressure phase diagram, and represents the discovery of a new phase within the V–C system.

In our recovered $\epsilon - VC_{y''}$ crystals, the c/a ratios all fall within the narrow range of 1.11–1.14, regardless of synthesis pressure. Figure 3 plots the fitted c/a ratios against the refined carbon occupancies from x-ray diffraction modeling, expressed in units of at.% C. To provide context for these values, data from a study of c/a versus carbon content in iron martensite are also plotted alongside our data [39]. In $\epsilon - VC_{y''}$, the c/a ratio is significantly higher than that seen in iron martensite (approx. 1.01 − 1.05), and it does not appear to vary significantly across the range of carbon concentrations present in our samples [39]. One interpretation is that the lattice has undergone the majority of its expansion at concentrations below ca. 10 at.% carbon, with additional carbon having minimal effect on c/a.

Figure 3 shows that there is not a direct linear transition from the bct to fcc structures between 0 and 50 at.% carbon. In other words, the addition of carbon does not lead to a linear increase in the c/a ratio up to the limit of full occupancy. This is already apparent from the fact that cubic VC_y samples have been stabilized with carbon concentrations as low as 37 at.% carbon [11]. It is notable that there appears to be a critical upper limit of carbon occupancy in $\epsilon - VC_{y''}$. From our data, we can estimate this limit to be around 27 at.% carbon. Taken together, these data suggest that over the range of around 27–37 at.% carbon, neither the $\epsilon - VC_{y''}$ nor the $B1$ phase is stable. It is perhaps no coincidence that this range aligns well with the known stability field of β-$V_2C_{y'}$ [11].

We performed calculations using density functional theory to evaluate how the tetragonal distortion from the cubic VC_y evolves with carbon content at zero pressure. These data are plotted as open circles in Figure 3, with the lowest energy structure at each composition plotted in red. The low-energy structures show good

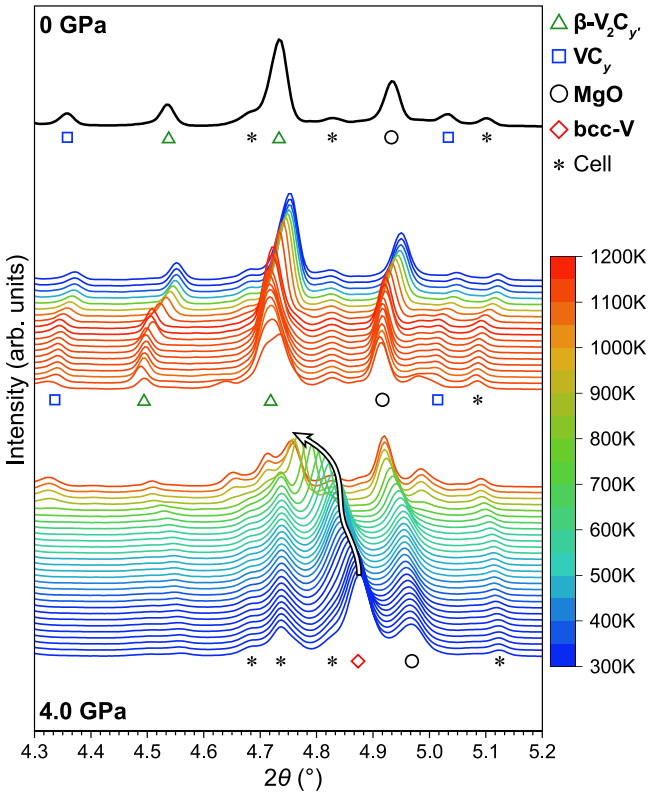

FIGURE 4 | Waterfall plot of the in situ XRD data collected during heating at 4.0 GPa. Prominent diffraction peaks from phases of interest are highlighted with various shapes as listed in the legend. The trajectory of the (110) peak of bcc-V is highlighted with a black outlined arrow. The patterns shown were collected every 100 s. The color of each trace indicates the temperature at the time of collection (see legend). The traces are separated around halfway to allow for clearer annotation of the peaks that appear. The topmost separated trace shows the diffraction pattern recorded at ambient pressure and temperature after decompression. Peaks arising from the sample cell assembly are all labeled with an asterisk for clarity.

agreement with the experimentally observed ratio below 27 at.% carbon. The calculations also capture the known preference for the NaCl-type structure at compositions above 37 at.% carbon. Under traditional synthesis conditions (i.e., at low pressures), the β-$V_2C_{y'}$ has long been known as the most metal-rich binary phase that can be stabilized within the V–C system. In this context, the $\epsilon - VC_{y''}$ phase represents the discovery of a new phase that is more metal-rich than any of the phases known to date. To gain deeper insight into the formation of the metastable $\epsilon - VC_{y''}$ phase, we turned to in situ x-ray diffraction collected during the synthesis runs.

3.3 | In Situ X-Ray Diffraction

In all four runs, we collected in situ x-ray diffraction data over the course of the experiment, providing a window into the evolution of the phases of interest during the reactions. Figure 4 plots a waterfall of integrated XRD patterns collected over the course of heating one of the samples after compressing to 4.0 GPa, focusing on a narrow range of 2θ for clarity. We describe one dataset here, but all four runs showed qualitatively the same behavior (see Supporting Information).

The low-temperature patterns clearly show diffraction from compressed bcc-V, as well as from various assembly components including MgO, TiB_2 (peak at around 5.1 °), and mullite. The lattice parameters of bcc-V were used to estimate pressure within the sample chamber, while the TiB_2 lattice parameters provided an estimate of pressure just outside the sample. Since pure bcc-V does not exist after the onset of reactions, we use the TiB_2 lattice parameters to approximate the pre-heating and postheating pressures in all runs reported here [40]. The MgO lattice parameters were also monitored as a marker of temperature increase and a rough estimate of pressure.

At the onset of heating, the unit cells of bcc-V and MgO both expand in accordance with their expected thermal expansion, which has been previously measured over the relevant pressure range for both phases [41, 42]. However, above approximately 800 K, the bcc-V peaks exhibit a significant departure from the expected thermal expansion behavior, rising to a unit cell volume much higher than could be expected from temperature increase alone. This trajectory is highlighted by a black curved arrow in Figure 4. One interpretation could be a significant drop in the sample pressure, but we did not observe the same dramatic lattice expansion for other phases present in the patterns, and we saw no drop in the hydraulic pressure in the press.

Another interpretation for the expansion of the bcc-V lattice is that it is caused by carbon diffusing into the interstitial sites. Indeed, this would be expected to cause an expansion of the lattice along with a concomitant decrease in sample pressure as the relatively low density graphite is consumed to form the high density bcc-derived vanadium carbide phase. At around the same time that the bcc-V lattice reaches its maximum volume, we observe the growth of peaks that can be readily attributed to β-$V_2C_{y'}$, as well as an additional set of weaker peaks. The weaker peaks are consistent with the known $B1$ VC_y structure.

After decompressing the sample slowly over 8 h to near ambient pressure, a final x-ray diffraction pattern was collected while the sample was still in the press. This pattern was used to extract lattice parameters for β-$V_2C_{y'}$ ($a = 2.89$, $c = 4.58$), which are in good agreement with those determined from the SCXRD studies described above. Although the weak peaks that we ascribe to the $B1$ phase were also present in this pattern, we did not observe single crystals of this phase upon recovery and we do not see evidence of this phase in the EBSD maps (vide infra). One possible interpretation is that the $B1$ phase can be stabilized at pressure with a much lower carbon content than has been previously observed, but then transforms at lower pressure into $\epsilon - VC_{y''}$. This would be consistent with the lack of diffraction peaks from the $\epsilon - VC_{y''}$ phase in these patterns, although we should note that many of its peaks are coincident with the β-$V_2C_{y'}$ and MgO phases and would therefore be obscured anyway. It is also important to note that even though the final in situ pattern was measured after decompression of the press, the sample may still be under residual high strain. The transition into the bct phase may thus be occurring later, when the assembly is fully removed from the press.

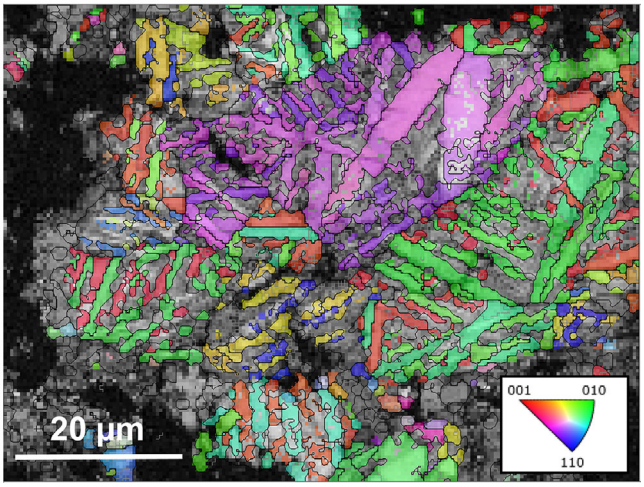

FIGURE 5 | Overlay of the band contrast and IPF map collected on the surface of a polished piece of the pellet recovered from 3.7 GPa. The IPF map is shown for the $\epsilon - VC_{y''}$ phase exclusively (orientation legend shown in the bottom right). The band contrast is shown in grayscale, where the brighter areas represent regions with higher diffraction intensities. High band contrast regions without IPF color overlays index primarily to bcc-V (see the Supporting Information).

3.4 | Phase and Crystal Orientation Mapping

We used EBSD to examine a polished surface of the sample pellet recovered from the 3.7 GPa synthesis. We saw little to no contribution from any other carbide/oxide phases, including the $B1$ phase (see Supporting Information). The majority of the sample surface was β-$V_2C_{y'}$ (75%), with the remainder being $\epsilon - VC_{y''}$ (23%) and bcc-V (2%). Figure 5 shows an inverse pole figure (IPF) map measured over the RD-TD rolling plane in a zoomed region containing a grain rich in both $\epsilon - VC_{y''}$ and bcc-V. The IPF map is shown for the $\epsilon - VC_{y''}$ phase exclusively, and reveals a lath or needle-like orientation of the $\epsilon - VC_{y''}$ phase within a bcc-V matrix. This texture is reminiscent of the characteristic laths observed in iron martensite, and may provide clues into how the $\epsilon - VC_{y''}$ phase is formed [43, 44]. Given that lath structures in martensitic iron steels are believed to form as a way to minimize internal stress during the diffusionless transformation from austenite (fcc) to martensite (bct), their presence here may be evidence of a similar diffusionless transition between the $B1$ phase and $\epsilon - VC_{y''}$.

4 | Conclusion

We have presented the first investigation into the reactivity of the V–C system at high pressures and temperatures. We recovered large single crystals of the previously known β-$V_2C_{y'}$ as well as single crystals of a novel phase, $\epsilon - VC_{y''}$, that can be described structurally as a carbon-rich analogue of iron martensite. A single crystal x-ray diffraction analysis of the recovered samples of β-$V_2C_{y'}$ was consistent with values reported in the literature in terms of both lattice parameters and carbon occupancy, suggesting a limited sensitivity of the carbon content to the synthesis pressure in this phase. In the single crystal x-ray diffraction of the novel $\epsilon - VC_{y''}$ phase, we observed a c/a ratio that was largely invariant over the broad range of carbon occupancies measured.

Our in situ XRD and ex situ EBSD data allow us to formulate a hypothesis for the chemical reactivity of vanadium and carbon under the elevated pressures studied here. First, above approximately 800 K, bcc-V undergoes a significant expansion of its lattice caused by the diffusion of carbon into its interstitial sites. This diffusion into the lattice continues with sustained heating until the carbon content is high enough, the expanded bcc-V begins to transform into β-$V_2C_{y'}$ and VC_y structures (the decrease in the bcc-V peak intensity supports this). While we do not see direct evidence for the $\epsilon - VC_{y''}$ phase in the in situ XRD data, the EBSD mapping suggests that the β-$V_2C_{y'}$ phase is retained all the way through quenching, whereas the tetragonally distorted $\epsilon - VC_{y''}$ phase may be arising from a diffusionless distortion of the carbon-poor VC_y phase. This would be an interesting mirroring of the diffusionless mechanism by which austenite transforms into martensite in the Fe–C system, and hints at a new method for the pressure processing of vanadium-based steels.

Acknowledgments

This work was funded by the National Science Foundation (DMR-2237478) and by an American Chemical Society Petroleum Research Fund grant (PRF66490). The authors gratefully acknowledge the Beneski SEM Laboratory at Amherst College, funded by the Amherst College Kresge Endowment Fund, for their support, and assistance in this work. Portions of this work were performed at the MAXPD endstation, supported by the National Science Foundation Division of Earth Sciences via SEES: Synchrotron Earth and Environmental Science (EAR-2223273), and by the Mineral Physics Institute, Department of Geosciences, Stony Brook University. This research used the XPD (28-ID-2) Beamline of the National Synchrotron Light Source II, a U.S. Department of Energy (DOE) Office of Science User Facility operated for the DOE Office of Science by Brookhaven National Laboratory under Contract No. DE-SC0012704. Crystal structures were rendered using Vesta 3.5.8. Data analysis and graphing of in situ XRD and single crystal data were performed using OriginPro 2022 (OriginLab Corporation, Northampton, MA, USA). This work was completed in part with resources provided by the University of Massachusetts' Green High Performance Computing Cluster (GHPCC).

Conflicts of Interest

The authors declare no conflict of interest.

References

1. L. Toth, *Transition Metal Carbides and Nitrides*, vol. 7, no. 1 (Academic Press, 2014).

2. W. S. Williams, "Transition-Metal Carbides," *Progress in Solid State Chemistry* 6 (1971): 57–118.

3. T. Kosolapova, *Carbides: Properties, Production, and Applications* (Springer US, 2012).

4. A. S. Kurlov and A. I. Gusev, "Phase Equilibria in the W–C System and Tungsten Carbides," *Russian Chemical Reviews* 75, no. 7 (2006): 617–636.

5. C. Aguzzoli, C. Aguzzoli, C. A. Figueroa, et al., "Corrosion and Nanomechanical Properties of Vanadium Carbide Thin Film Coatings of Tool Steel," *Surface and Coatings Technology* 206, no. 10 (2012), https://doi.org/10.1016/J.SURFCOAT.2011.11.042.

6. Y. Dall'Agnese, P.-L. Taberna, Y. Gogotsi, and P. Simon, "Two-Dimensional Vanadium Carbide (mxene) as Positive Electrode for

Sodium-Ion Capacitors," *The Journal of Physical Chemistry Letters* 6, no. 12 (2015): 2305–2309.

7. Y. Krutskii, T. Gudyma, I. Kuchumova, R. Khabirov, and K. Antropova, "Carbides of Transition Metals: Properties, Application and Production. Review. Part 1. Titanium and Vanadium Carbides," *Izvestiya Ferrous Metallurgy* 65 (2022): 305–322, https://fermet.misis.ru/jour?locale=en_US.

8. T. N. Baker, "Processes, Microstructure and Properties of Vanadium Microalloyed Steels," *Materials Science and Technology* 25, no. 9 (2009): 1083–1107.

9. J. Takahashi, K. Kawakami, and Y. Kobayashi, "Origin of Hydrogen Trapping Site in Vanadium Carbide Precipitation Strengthening Steel," *Acta Materialia* 153 (2018): 193–204.

10. J. Lee, T. Lee, Y. J. Kwon, D.-J. Mun, J.-Y. Yoo, and C. S. Lee, "Effects of Vanadium Carbides on Hydrogen Embrittlement of Tempered Martensitic Steel," *Metals and Materials International* 22, no. 3 (2016): 364–372.

11. V. N. Lipatnikov, "Phase Equilibria, Phases and Compounds in the V—C System," *Russian Chemical Reviews* 74, no. 8 (2005), https://doi.org/10.1002/CHIN.200606238.

12. O. N. Carlson, A. H. A. Ghaneya, and J. F. Smith, "The C-V (Carbon-Vanadium) System," *Bulletin of Alloy Phase Diagrams* 6 (1985): 115–124.

13. W. Xing, F. Meng, and R. Yu, "A New Type of Vanadium Carbide V_5C_3 and Its Hardening by Tuning Fermi Energy," *Scientific Reports* 6, no. 1 (2016), https://doi.org/10.1038/SREP21794.

14. Y. Hou, S. Otani, T. Tanaka, and Y. Ishizawa, "Preparation of Vanadium Carbide Single Crystals by a Floating Zone Technique," *Journal of Crystal Growth* 68, no. 3 (1984): 733–740.

15. R. Kapoor, "Synthesis, Reactivity, and Thermochemistry of Vanadium Carbide and Nitride" (PhD diss., Clarkson University, 1994).

16. G. H. Emmons, "Thermodynamic Study of Order–Disorder Transitions in Vanadium Carbide" (PhD diss., University of Illinois at Urbana, 1972).

17. C. R. Weinberger and G. B. Thompson, "Review of Phase Stability in the Group IVb and Vb Transition-Metal Carbides," *Journal of the American Ceramic Society* 101, no. 10 (2018): 4401–4424, https://doi.org/10.1111/JACE.15768.

18. S. D. Thiel and J. P. S. Walsh, "First-Principles Investigation of Phase Stability in Substoichiometric Zirconium Carbide Under High Pressure," *Advanced Theory and Simulations* 5, no. 12 (2022): 2200439.

19. Y. Zhong, X. Xia, F. Shi, J. Zhan, J. Tu, and H. J. Fan, "Transition Metal Carbides and Nitrides in Energy Storage and Conversion," *Advanced Science* 3, no. 5 (2016): 1500286.

20. A. Kurlov, A. Gusev, E. Y. Gerasimov, I. Bobrikov, A. Balagurov, and A. Rempel, "Nanocrystalline Ordered Vanadium Carbide: Superlattice and Nanostructure," *Superlattices and Microstructures* 90 (2016): 148–164.

21. C. R. Weinberger and G. B. Thompson, "The Crystal Structure and Phase Stability of the Zeta Phase in the Group VB Transition Metal Carbides: A Computational Investigation," *Acta Crystallographica Section B* 75, no. 5 (2019): 870–879.

22. L. Fleischer and J. Tobin, "Growth of Transition Metal Carbide Single Crystals by Recrystallization: I. Preparation of Fully-Dense Transition Metal Carbide," *Journal of Crystal Growth* 8, no. 3 (1971): 235–242.

23. S. T. Oyama, *Introduction to the Chemistry of Transition Metal Carbides and Nitrides* (Springer Netherlands, 1996), 1–27.

24. J. Chen, F. Peng, Y. Wang, et al., "Mechanisms and Mechanical Properties of High-Temperature High-Pressure Sintered Vanadium Carbide Ceramics," *International Journal of Refractory Metals and Hard Materials* 118 (2024): 106483.

25. Leinenweber, J. Tyburczy, T. Sharp, et al., "Cell Assemblies for Reproducible Multi-Anvil Experiments (The Compres Assemblies)," *American Mineralogist* 97 (2012): 535.

26. K. Leinenweber, J. Mosenfelder, T. Diedrich, et al., "High-Pressure Cells for In Situ Multi-Anvil Experiments," *High Pressure Research* 26, no. 3 (2006): 283–292.

27. O. V. Dolomanov, L. J. Bourhis, R. J. Gildea, J. A. Howard, and H. Puschmann, "Olex2: A Complete Structure Solution, Refinement and Analysis Program," *Journal of Applied Crystallography* 42, no. 2 (2009): 339–341.

28. G. M. Sheldrick, "Shelxt–Integrated Space-Group and Crystal-Structure Determination," *Acta Crystallographica Section A: Foundations and Advances* 71, no. 1 (2015): 3–8.

29. S. J. Clark, M. D. Segall, C. J. Pickard, et al., "First Principles Methods using CASTEP," *Zeitschrift für Kristallographie* 220, no. 5-6 (2005): 567–570.

30. J. P. Perdew, K. Burke, and M. Ernzerhof, "Generalized Gradient Approximation Made Simple," *Physical Review Letters* 77, no. 18 (1996): 3865–3868.

31. H. J. Monkhorst and J. D. Pack, "Special Points for Brillouin-Zone Integrations," *Physical Review B* 13, no. 12 (1976): 5188.

32. A. Hjorth Larsen, J. Jørgen Mortensen, J. Blomqvist, et al., "The Atomic Simulation Environment—A Python Library for Working With Atoms," *Journal of Physics: Condensed Matter* 29, no. 27 (2017): 273002.

33. S. P. Ong, W. D. Richards, A. Jain, et al., "Python Materials Genomics (Pymatgen): A Robust, Open-Source Python Library for Materials Analysis," *Computational Materials Science* 68 (2013): 314–319.

34. G. B. Thompson and C. R. Weinberger, *Tantalum Carbides* (John Wiley & Sons, Ltd, 2014), ch. 12, 291–315.

35. A. S. Kurlov and A. I. Gusev, "Phase Transitions in the Lowest Tungsten Carbide W_2C," *Doklady Physics* 52, no. 12 (2007): 656–662.

36. P. V. Marshall, S. D. Thiel, E. E. Cote, J. Arigbede, M. L. Whitaker, and J. P. S. Walsh, "High-Pressure Synthesis and Recovery of Single Crystals of the Metastable Manganese Carbide, MnC_x," *Chemistry-A European Journal* 30 (2024): e202401581.

37. D. Hicks, M. J. Mehl, M. Esters, et al., "The Aflow Library of Crystallographic Prototypes: Part 3," *Computational Materials Science* 199 (2021): 110450.

38. T.-W. Liu and X.-L. Wu, "Martensitic Transformation Pathways and Crystallographic Orientation Relationships in Steel," *Journal of Materials Science & Technology* 174 (2024): 74–84.

39. T. Liu, L. Liang, D. Raabe, and L. Dai, "The Martensitic Transition Pathway in Steel," *Journal of Materials Science & Technology* 134 (2023): 244–253.

40. S. Ono and T. Kikegawa, "Titanium Boride Equation of State Determined by In-Situ X-Ray Diffraction," *Heliyon* 2, no. 12 (2016): e00220.

41. W. A. Crichton, J. Guignard, E. Bailey, D. P. Dobson, S. A. Hunt, and A. R. Thomson, "High-Temperature Equation of State of Vanadium," *High Pressure Research* 36, no. 1 (2016): 16–22.

42. J. Zhang, "Effect of Pressure on the Thermal Expansion of Mgo up to 8.2 Gpa," *Physics and Chemistry of Minerals* 27, no. 3 (2000): 145–148.

43. Z. Wang, H. Sun, X. Guo, et al., "Tempering Mechanism of Lath Martensite Induced in If Steel Under High Pressure," *Journal of Materials Science and Technology* 160 (2023): 148–160.

44. G. Miyamoto, N. Iwata, N. Takayama, and T. Furuhara, "Mapping the Parent Austenite Orientation Reconstructed From the Orientation of Martensite by EBSD and Its Application to Ausformed Martensite," *Acta Materialia* 58, no. 19 (2010): 6393–6403.

Supporting Information

Additional supporting information can be found online in the Supporting Information section.

Supporting File: chem70987-sup-0001-SuppMat.pdf